Materials Science & Engineering A 606 (2014) 380–389

Contents lists available at ScienceDirect

Materials Science & Engineering A

journal homepage: www.elsevier.com/locate/msea

Grain refinement in a Cu–Cr–Zr alloy during multidirectional forging

I. Shakhova *, Z. Yanushkevich, I. Fedorova, A. Belyakov, R. Kaibyshev

Belgorod State University, Pobeda 85, Belgorod 308015, Russia

ARTICLE INFO

Article history:
Received 24 December 2013
Received in revised form
12 March 2014
Accepted 25 March 2014
Available online 2 April 2014

Keywords:
Cu–Cr–Zr alloy
Large strain deformation
Grain refinement
Precipitation
EBSD

ABSTRACT

Structural changes during plastic deformation were studied in a Cu–0.3%Cr–0.5%Zr alloy subjected to multidirectional forging up to a total strain of 4 at the temperatures of 300 K and 673 K. The deformation behavior was characterized by a rapid increase in the flow stress at an early deformation followed by a steady-state flow at large strain. The development of the new ultrafine grains resulted from the progressive increase in the misorientations of the strain-induced low-angle boundaries, which evolve into high-angle boundaries with increasing cumulative strain through a strain-induced continuous reaction that is quite similar to continuous dynamic recrystallization. The formation of ultrafine grains was closely related to the development of geometrically necessary boundaries that is attributed to deformation banding. The grain refinement kinetics increased with an increase in the deformation temperature. At 673 K, the area fractions of the ultrafine grains with a size below 2 μm were 0.36 and 0.6 in the initially solution treated samples and the aged samples, respectively. However, the area fractions of the ultrafine grains did not exceed 0.2 at 300 K.

1. Introduction

Copper and its alloys are widely used in various functional and structural applications, which frequently require both a high electrical conductivity and a high mechanical strength [1–3]. The strength of copper can be significantly increased by cold working [3–5], grain refinement [6–11], and the precipitation of nanoscale dispersoids [2,11–15]. However, strengthening leads to a pronounced decrease in the electrical conductivity, due to increase in the dislocation density, grain boundaries, dispersoids, and solutes, which increase the scattering of conducting electrons [1]. Thus, most of the high strength copper alloys exhibit a relatively low electric conductivity.

Recently, a promising approach for strengthening of Cu–Cr–Zr alloys while retaining their electric conductivity at a sufficiently high level of 80% IACS was developed [15–17]. This approach involves a large strain deformation followed by a final aging that enables the formation of an ultrafine-grained structure stabilized by nanoscale precipitations. The contributions of dispersoids and grain boundaries to the reduction of electrical conductivity are the lowest among all the aforementioned defects [1,13–15]. At the same time, dispersoids and grain boundaries provide an ultimate tensile strength of 600 MPa or higher through dispersion hardening and grain size strengthening [11,16]. Currently, this combination of strength and conductivity provided by the superposition of ultrafine-grained (UFG) structure, nanoscale coherent dispersoids and low-solute-content copper containing only traces of Cr and Zr is one of the best for copper and copper alloys.

The distribution of secondary phase particles in the Cu–Cr–Zr alloys has been considered in several works [2,12,13,18–22]. It was assumed [12–14,19] that the high electrical conductivity is due to the very low solubility of Cr and Zr in Cu, whereas the excellent strength is attributed to dispersion hardening by the nanoscale precipitates. There is no doubt that the strength/conductivity properties of the Cu–Cr–Zr alloys result from precipitation behavior during aging at 723–773 K. The following precipitation sequence for coherent Cr-rich phase particles was revealed in a dilute Cu–Cr alloy [18,23]: (i) Cr-rich fcc spherical precipitates, which can be considered as Guinier–Preston zones; (ii) coherent round/elliptical shaped bcc precipitates of B2-type structure having a Nishiyama–Wassermann orientation relationship with copper matrix and a size of 10 nm or less; (iii) plate/round shaped bcc precipitates having a Kurdjumov–Sachs orientation relationship with copper and a size of ~10 nm or higher. In ternary Cu–Cr–Zr alloys, the nanoscale particles of the Heusler phase $CrCu_2Zr$ belonging to the space group of Fm3m and having a Fe_3Al lattice and equiaxed shape precipitate instead of the Cr-rich bcc phase [13]. The Heusler phase exhibits a Nishiyama–Wassermann orientation relationship with the copper matrix [13]. At 823–873 K, this phase can decompose into two different phases of Cu_4Zr and Cr-rich bcc [13,24]. In addition, coarse precipitates of several Zr-rich phases (Cu_5Zr) and Cr-rich phases could form at grain boundaries and in grain interiors during solidification of the Cu–Cr–Zr alloys [19]. These particles do not dissolve during solution treatment if

* Corresponding author. Tel.: +7 4722 585457; fax: +7 4722 585417.
E-mail address: shakhova@bsu.edu.ru (I. Shakhova).

http://dx.doi.org/10.1016/j.msea.2014.03.116
0921-5093/

the Cr+Zr content exceeds the equilibrium solubility of Cr and Zr [19]. Thus, the finely dispersed coherent particles of bcc Cr or the Heusler phase precipitated due to the decomposition of supersaturated solid solution are the main contributors to the strengthening [18–22]. Concurrently, Cr and Zr deplete the copper matrix and hence provide high electric conductivity.

The grain refinement by large strain deformation provides structural strengthening consistent with the Hall–Petch relationship [25–29]. Recently, many techniques of severe plastic working, such as accumulative roll-bonding [11], equal channel angular pressing [7–10,16,17,28–31] and high pressure torsion [31–33], were applied to produce UFG structure in Cu–Cr–Zr alloys. It was shown that the high pressure torsion is the most effective technique in refining the grains and producing the large fraction of nanoscale grains after relatively small strains, whereas the equal channel angular pressing leads to only a partial UFG structure even after a cumulative true strain of $\varepsilon \sim 16$ [7–10,16,17,28–31]. There was no attempt to use multidirectional forging (MDF) for the grain refinement of Cu–Cr–Zr alloys despite the fact that this technique was highly efficient in producing UFG structure in copper at both room and intermediate temperatures [34,35]. The MDF technique is one of the simplest methods, which allows processing of large-scale products of rather ductile materials and does not require a strictly specialized equipment [34–36]. Another advantage of MDF is the possibility to analyze the stress–strain behavior of the processed material directly during SPD.

The formation of UFG structures in copper during large strain deformation results from a type of continuous dynamic recrystallization (CDRX), in which grain refinement can be considered as an evolution of the deformation substructures [10,34–39]. At low temperatures, the low-angle misorientations are initially introduced by deformation banding [10,34,35]. Next, accumulation of lattice dislocations by low-angle boundaries (LABs) and their arrangement within the boundaries of the deformation bands [10,40] lead to the gradual transformation of LABs into high-angle boundaries (HABs), resulting in the formation of UFG structure after sufficiently large strains [34,35]. Therefore, different deformation structures in the form of deformation bands, subgrain structure, partially recrystallized structure and fully UFG structure may evolve during MDF with increasing strain [34,35]. The aim of the present study is to investigate the sequence of structural changes that result in grain refinement in a Cu–Cr–Zr alloy during cold-to-warm MDF. The paper also aims to clarify the effects of processing temperature and dispersed particles on the grain refinement kinetics.

2. Materials and experimental procedure

An experimental alloy of Cu–0.3%Cr–0.5%Zr (wt%) was examined in the present work. The specimens were subjected to a solution treatment at 1193 K for 30 min, followed by water quenching. These samples are denoted as ST. A part of the ST samples was aged at 723 K for 1 h with subsequent water quenching. These aged Cu–Cr–Zr samples are denoted as AT.

The rectangular samples with starting dimensions of 25 mm × 20 mm × 16 mm were machined for MDF. The MDF was performed using an Instron300LX machine equipped with a three-sectioned high temperature furnace. The dimensional ratio of the MDF specimens (1.5 × 1.22 × 1.0) was not changed during the MDF, while the loading axis was changed through 90° from pass to pass, and a true strain of ~0.4 was imposed to the material in each forging pass. Both the ST and AT samples were subjected to MDF at both 300 K and 673 K under a strain rate of approx. $10^{-3}\ s^{-1}$. The microhardness was studied using the Vickers test with a load of 300 g and an exposure time of 10 s. The electrical conductivity was measured using a four-point bridge technique.

Microstructural investigations were performed on the sections parallel to the final forging axis using a Quanta 600 FEG scanning electron microscope equipped with an electron backscattering diffraction (EBSD) analyzer incorporating an orientation-imaging microscope (OIM) and a Jeol JEM-2100 transmission electron microscope equipped with an INCA X-ray energy-dispersive spectrometer. The specimens for the EBSD analysis were electrochemically polished at room temperature using an electrolyte of HNO_3:CH_3OH = 1:3. The step size for the EBSD scan was 100 nm for the samples strained to $\varepsilon \sim 1.2$ and 55 nm for samples strained to $\varepsilon \sim 2$ and ~4. The OIM images were subjected to clean-up procedures, setting a minimal confidence index of 0.1. An average grain size (D) was estimated using the linear intercept method on the OIM images for the distance between the HABs (10 orthogonal lines for each image). A critical misorientation angle between the LABs and HABs was chosen at 15°. The UFG area fraction and the HAB fraction were obtained by using OIM software (EDAX TSL, version 5.2). Foils for TEM investigations were mechanically thinned and then electro-polished using the aforementioned electrolyte at temperature −15 °C using a Tenupol 5 twinjet polishing unit. The subgrain size (d) was estimated by the linear intercept method on the TEM micrographs counting all the clear visible boundaries/subboundaries. The dislocation density was measured by counting the individual dislocations within the grain/subgrain interiors in at least 5 arbitrarily selected TEM images for each data point [41].

3. Results

3.1. Initial microstructure

The alloy initially had an average grain size of ~700 μm (Fig. 1a) and a low dislocation density of $\rho \sim 3 \times 10^{12}\ m^{-2}$. At 1193 K, Zr and Cr did not dissolve completely and the particles with an average size of ~150 nm were present in the ST states (Fig. 1b). The aging led to precipitation of tiny bcc chromium particles having round shapes and sizes less than 10 nm. These particles exhibited the Nishiyama–Wassermann orientation relationship with the copper matrix (Fig. 1c). The specific contrast on the TEM image of these particles suggested their coherent origin and high coherent stress. No evidence was found for the precipitation of the Heusler phase of $CrCu_2Zr$, which could be distinctly recognized by the diffraction pattern.

3.2. Stress–strain behavior

The true stress–strain curves for the ST and AT samples are plotted for 10 consecutive forging passes at the temperatures of 300 K and 673 K in Fig. 2. The temperature and material conditions insignificantly affected the shape of the envelope flow curves. In general, extensive strain hardening occurs at an early deformation; the flow stress rapidly increases by over twofold during the first pass. The strain hardening gradually decreases with increasing strain. Some of the forging passes are characterized by an apparent strain softening, which can be attributed to the change in the strain path caused by strain localization [42]. The envelope curve of the flow stress increases to a maximum with an increase in the cumulative strains to ~1.5, followed by apparent steady-state behavior at larger cumulative strains. At 673 K, the flow stresses of the ST and AT samples are almost the same, whereas at 300 K, the AT samples exhibit significantly higher flow stresses than those of the ST samples. Note that there is no remarkable difference between the yield stress at reloading and the flow stress just before unloading. Therefore, there is no

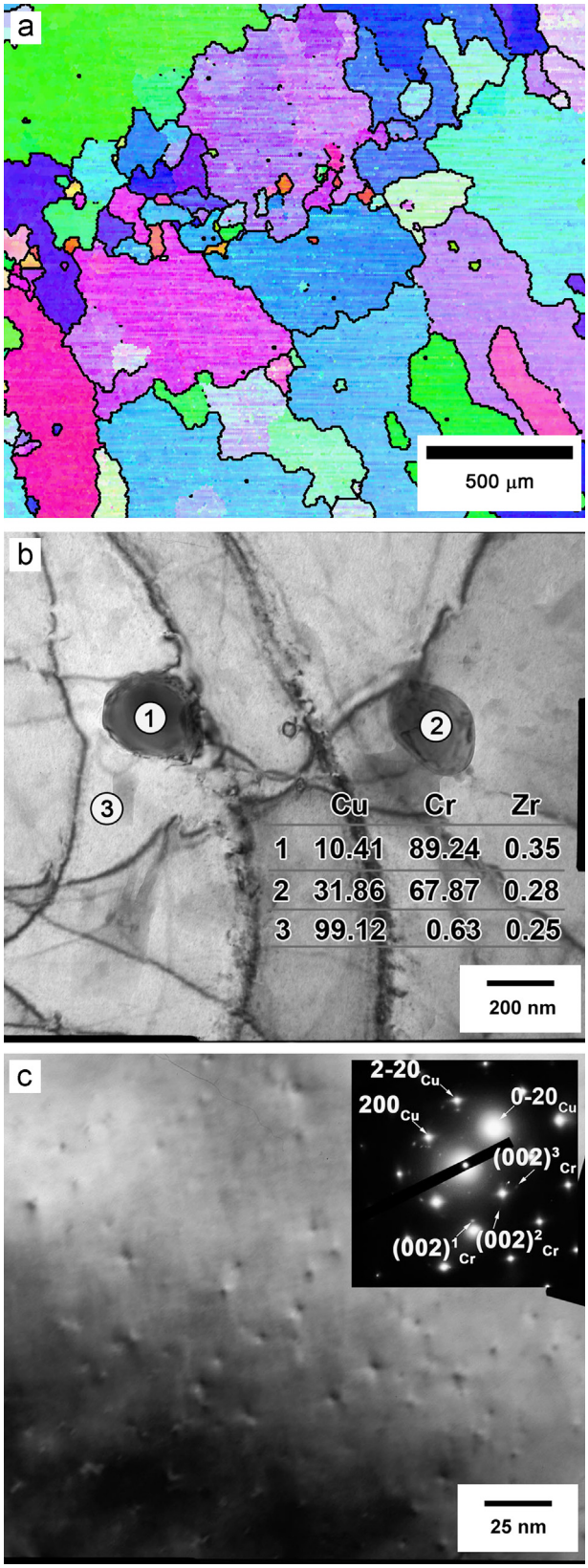

Fig. 1. Fine sub-microstructure in the as-cast (a), the solution treated (ST) (b), and aging treated (AT) (c) Cu–Cr–Zr samples. The table insets show the chemical composition in wt% of the indicated areas.

evidence for any static recrystallization processes [43,44] during the MDF; in addition, the microstructure evolution during the MDF occurs in a continuous manner as a result of strain accumulation.

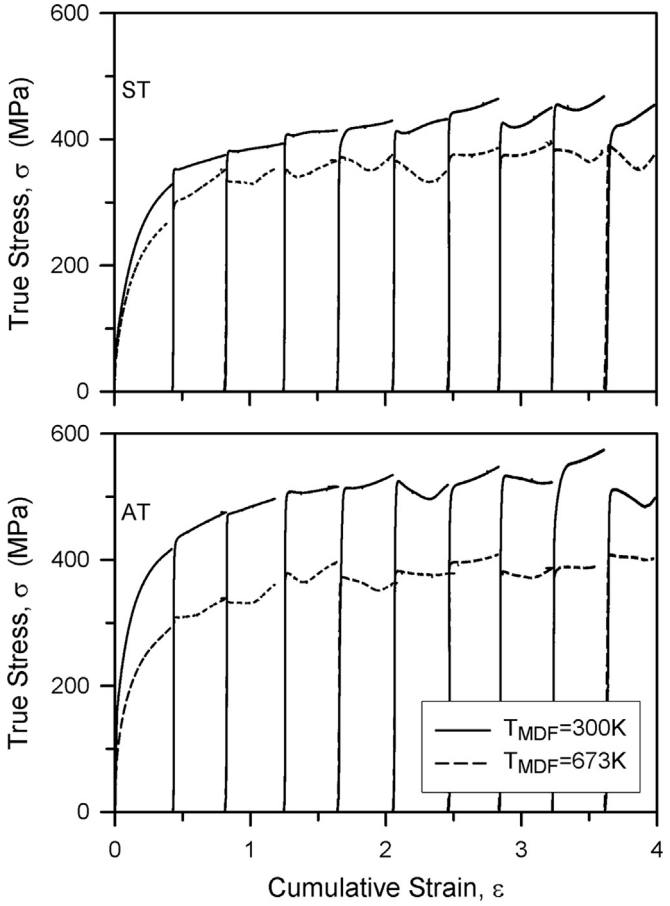

Fig. 2. The true stress–strain curves in the solution treated (ST) (a) and aging treated (AT) (b) Cu–Cr–Zr samples obtained during multidirectional forging at 300 K and 673 K under a strain rate of $10^{-3}\,s^{-1}$.

3.3. Deformation microstructures

3.3.1. Microstructure evolution in the solution treated state

Typical deformation microstructures that developed in the ST state are shown in Figs. 3 and 4. A spatial net of the LABs evolved during MDF to relatively small strains at 300 K (Fig. 3a). The deformation subboundaries are represented by numerous strain-induced planar dislocation subboundaries (Fig. 4a). Further straining is accompanied by an increase in the misorientation of the strain-induced dislocation subboundaries. The formation of micron-scale grains entirely delimited by HABs occurring at $\varepsilon \sim 2$ (Fig. 3b). The number of UFGs increases during subsequent MDF, leading to a necklace-like microstructure consisting of chains of UFGs surrounding coarse remnants of the original grains (Fig. 3c). The new grains resulted from the gradual evolution of the deformation subgrains. The formation of planar dislocation subboundaries with low-angle misorientations occurs at relatively small strains (Fig. 4b). With increasing strain, the highly elongated subgrains become subdivided by transverse subboundaries, thereby increasing the subboundary misorientations. This behavior results in the formation of more-or-less equiaxed crystallites/subgrains bounded by low-to-high-angle boundaries (Fig. 4c).

It is clearly seen in Fig. 3d that a great number of deformation bands delimited by HABs develop at 673 K after straining to $\varepsilon \sim 1.2$. Further MDF is accompanied by the formation of UFGs, the volume fraction of which increases with an increase in the total strain (Fig. 3e and f). The appearance of the strain-induced HABs is closely connected with the development of the deformation bands

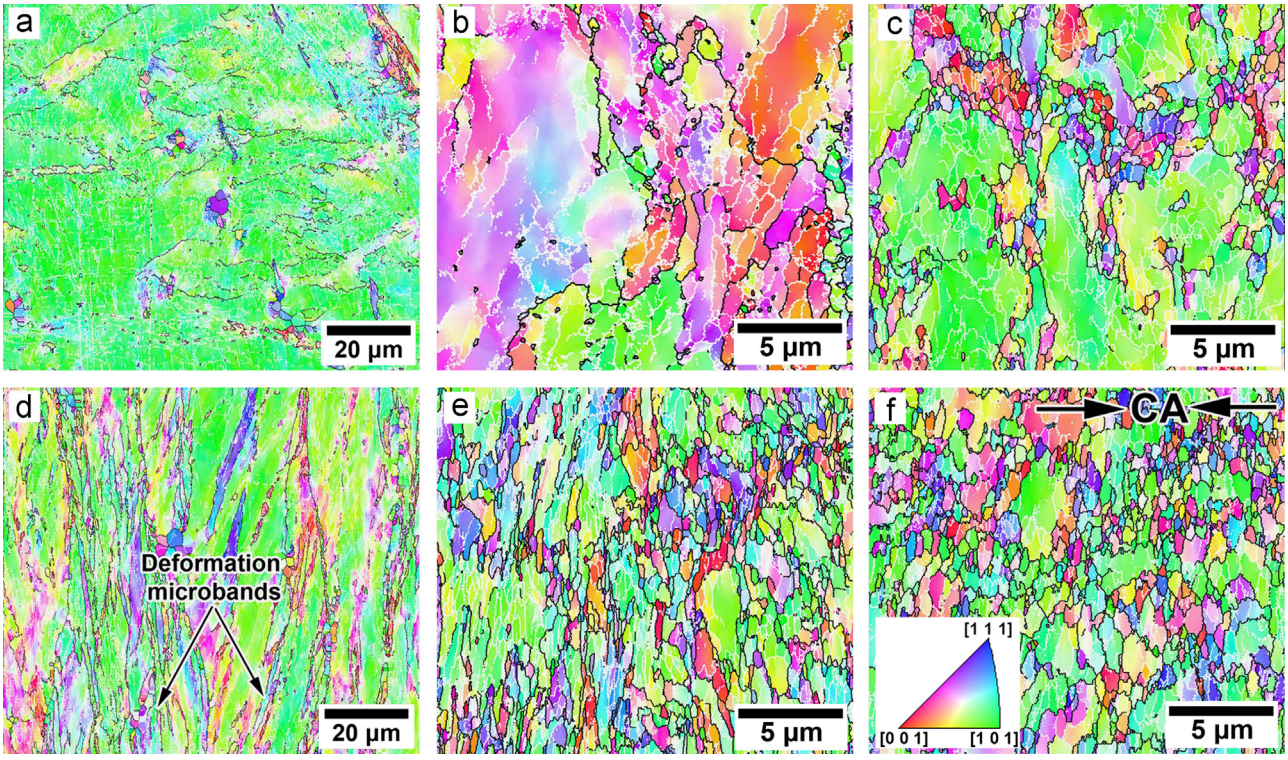

Fig. 3. Typical microstructures developed in the Cu–Cr–Zr alloy in quenched condition (ST) subjected to multidirectional forging at 300 K (a–c) and 673 K (d–f) to a total strain of 1.2 (a, d); 2 (b, e); 4 (c, f). The white and black lines indicate the low- ($\theta < 15^{\circ}$) and high-angle ($\theta \geq 15^{\circ}$) boundaries, respectively. The inset in (f) shows the inverse pole figures for the compression axes (CA) in the last compression pass.

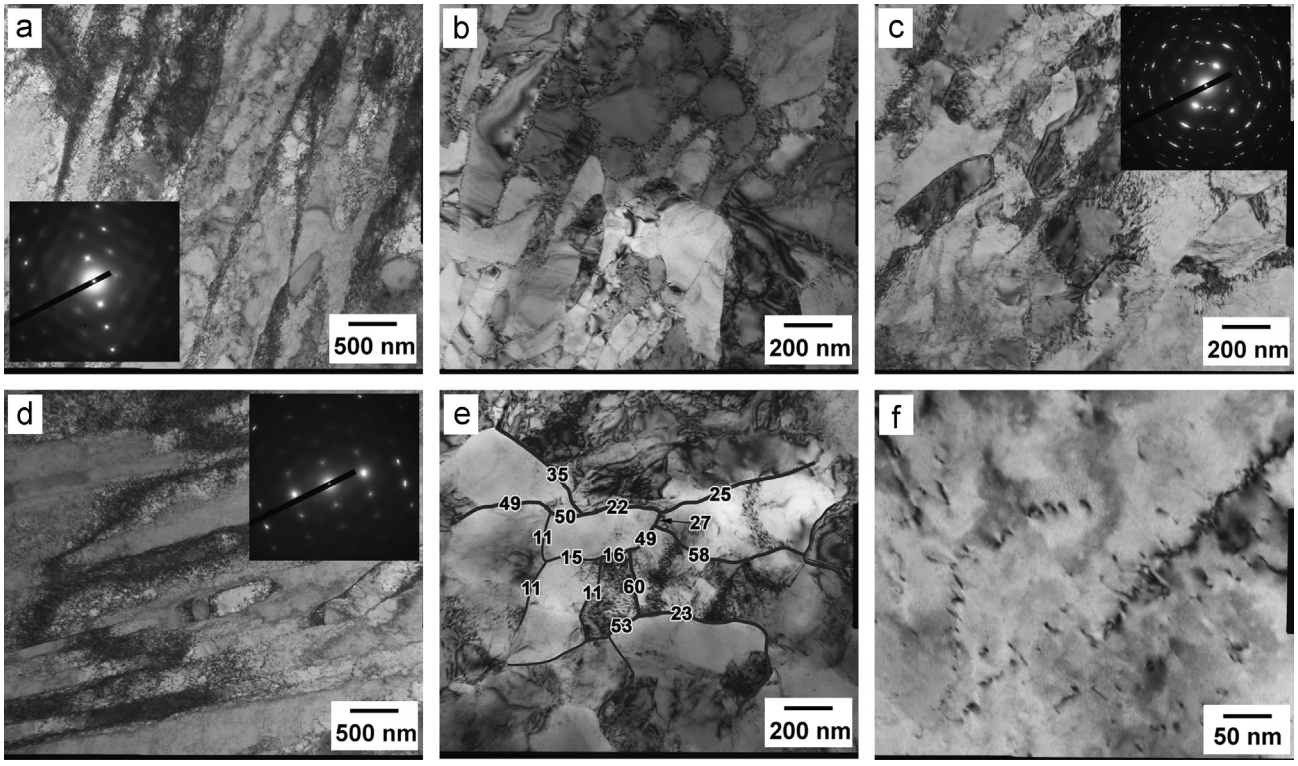

Fig. 4. Typical TEM micrographs of the Cu–Cr–Zr alloy in quenched condition (ST) subjected to multidirectional forging at 300 K up to total strains of 0.4 (a); 2 (b); 4 (c) and at 673 K to total strains of 0.4 (d); 4 (e); and 2 (f).

crossing over the interiors of the original grains. The partially recrystallized microstructure, which contains the fine grains and the crystallites/subgrains subdivided by LABs, develops after a large cumulative strain of ~4. The deformation substructures developed at relatively small strains consist of closely spaced planar dislocation subboundaries with low-angle misorientations (Fig. 4d). The spacing of these subboundaries is significantly smaller in comparison with the MDF at 300 K (cf. Fig. 4a and d).

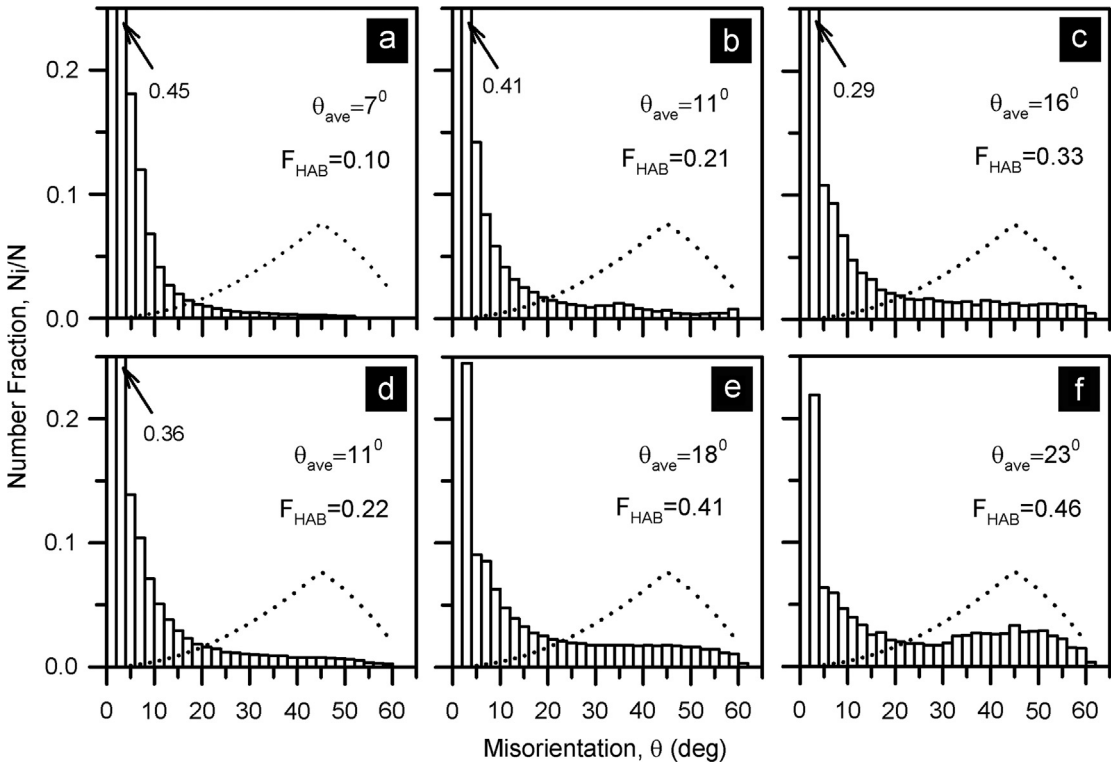

Fig. 5. Misorientation distributions of grain/subgrain boundaries in the Cu–Cr–Zr alloy in quenched condition (ST) subjected to multidirectional forging at 300 K (a–c) and 673 K (d–f) to a total strain of 1.2 (a, d); 2 (b, e); and 4 (c, f).

Therefore, an increase in the temperature from 300 to 673 K leads to an increase in the density of strain-induced planar boundaries and their misorientations. Subsequent MDF results in the development of transverse subboundaries among the planar dislocation substructure, leading to the formation of nearly equiaxed crystallites/grains bounded by low-to-high-angle boundaries (Fig. 4e). Note that nanoscale coherent dispersoids precipitated in the ST state during MDF at 673 K (Fig. 4f).

Fig. 5 shows the misorientation distributions for the grain/subgrain boundaries along with the average misorientation angle (θ_{ave}) and the fraction of HABs (F_{HAB}) for the ST samples subjected to MDF at different temperatures. The misorientation distributions that developed at a relatively small strain of 1.2 are characterized by the sharp peaks against small angles, and the boundary fractions gradually decrease to almost zero with increasing misorientation angle. It should be noted that rather high values of F_{HAB} and θ_{ave} were observed in the sample strained at 673 K. This can be associated with the deformation microband evolution, which results in rapid development of HABs. Commonly, the fractions of small misorientations decrease with increase in the strain. Correspondingly, the average boundary misorientation and the fraction of HABs progressively increase during MDF. Both the θ_{ave} and F_{HAB} increase faster during MDF at higher temperature. The portion of misorientation distribution above 15° evolved at $\varepsilon\sim4$ at 673 K is composed of almost the same fractions of various misorientations with a small maximum against 45° that is similar to random misorientation distribution [45] indicated by the dotted line in Fig. 5.

The strain and temperature effects on the change of some microstructural parameters, i.e., the mean grain size (D), the transverse subgrain (d) size, the dislocation density (ρ), the fraction of HABs (F_{HAB}), and the area fraction of UFGs having grain sizes below 2 μm (F_{UFG}), during MDF of the ST state are shown in Fig. 6. The mean grain size reduces by approximately two orders-of-magnitude after five MDF passes. Then, the rate of grain refinement slows down upon subsequent MDF, resulting in the final grain sizes of 1.4 μm and 0.9 μm at 300 K and 673 K, respectively. Note that at 673 K, the MDF leads to a finer grain size at all strains compared to the grain size at ambient temperature. The most remarkable difference between the deformed structures evolved at different temperatures is observed at $\varepsilon\sim2$, when the grain sizes are approximately 5 μm and 1 μm at 300 K and 673 K, respectively. In contrast, the changes in the transverse subgrain size are almost independent of strain. The evolution of the dislocation density in the grain/subgrain interiors behaves similar to the transverse subgrain size. An increase in the total strain is accompanied by a small increase in the dislocation density, and a lower MDF temperature results in a higher dislocation density.

Grain refinement can be followed by an increase in the fraction of HABs and the area fraction of UFGs, as shown in Fig. 6. At 300 K, the fraction of HABs increases almost linearly with the total strain, approaching 0.33 at $\varepsilon\sim4$. At 673 K, the F_{HAB} demonstrates a more rapid linear increase with strain than at 300 K, approaching 0.41 at $\varepsilon\sim2$. Subsequently, the kinetics of the HAB formation slow down, leading the F_{HAB} to reach 0.46 at $\varepsilon\sim4$. Generally, the increase in the fraction of strain-induced HABs should correlate with the development of the UFGs, because the new grains form as a result of the increase in the subboundary misorientation brought about by continuous accumulation of the dislocations introduced by the deformation. The progress in the development of the UFGs is represented in Fig. 6 by the area fraction of the grains with a grain size below 2 μm. The appearance of the UFGs occurs when the cumulative strain exceeds 1.2. Further MDF at 300 K is accompanied by a gradual increase in the F_{UFG}, which attains a value of 0.2 at $\varepsilon\sim4$. However, at 673 K, the rapid enlargement of the UFG fraction occurs in the strain range of $1.2<\varepsilon<2$, where the F_{UFG} increases to 0.3. Then, similar to the HAB fraction, the F_{UFG} exhibits a slow increase to 0.36 upon subsequent MDF to $\varepsilon\sim4$.

3.3.2. *Microstructure evolution in the state after the aging treatment*

The deformation microstructures of the AT samples are shown in Figs. 7 and 8. The sequence of the structural changes in these samples during MDF is similar to that observed in the ST state. Namely, the

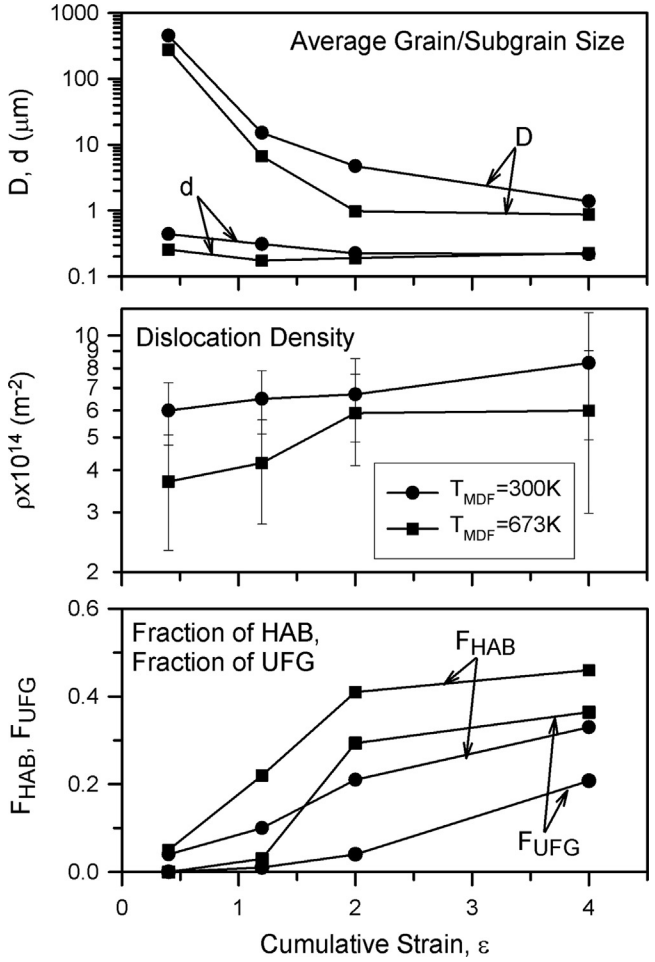

Fig. 6. Effect of multidirectional forging at 300 K and 673 K on the structural parameters (the average grain/(sub)grain size (D, d), the dislocation density (ρ), the fraction of HAB (F_{HAB}) and the fraction of ultrafine grains (F_{UFG})) in the solution treated (ST) state of a Cu–Cr–Zr alloy.

MDF at 300 K results in the development of low-angle planar dislocation subboundaries (Fig. 8a), some of which rapidly increased their misorientations and became HABs (Fig. 7a). Further deformation is accompanied by the subdivision of highly elongated subgrains by the formation of transverse subboundaries that results in the evolution of near equiaxed subgrains (Fig. 8b), the misorientations among which increase during subsequent MDF. Thus, the development of boundaries with low-to-high-angle misorientations, i.e., an increase in their density and misorientations, leads to the formation of the UFGs, the number of which gradually increases with straining (Fig. 7b and c). A dispersion of the secondary phase remains essentially unchanged during MDF (Fig. 8c).

The temperature of the MDF highly accelerates the rate of grain refinement. At 673 K, the spatial networks of the planar LABs evolve within the initial grains at $\varepsilon\sim1.2$ (Fig. 7d). The formation of numerous elongated UFGs at $\varepsilon\sim2$ is clearly seen in Fig. 7e. The fraction of the UFGs rapidly increases with straining, although rather coarse remnants of the original grains can be observed, even at $\varepsilon\sim4$ (Fig. 7f). In contrast to the other samples, the deformation substructures developed in the AT samples at 673 K are characterized by more equiaxed subgrains at relatively small strains (Fig. 8d). The misorientations of the deformation subboundaries increase, leading to the development of largely misoriented crystallites/subgrains upon further deformation (Fig. 8e and f). Therefore, the main distinctive feature of the AT samples from the ST samples is associated with the homogeneity of the deformation at intermediate strains at 673 K. At $\varepsilon\sim1.2$, the more uniform deformation structure evolves in the AT samples but not in the ST samples (cf. Figs. 3d and 7d). Then, the new UFGs appear homogeneously in the AT samples upon further MDF, leading to a rapid increase in the fraction of the UFGs (Fig. 7e and f).

The grain boundary misorientation distributions that developed in the AT samples during MDF at 300 and 673 K (Fig. 9) are quite similar to those in the ST state (Fig. 5). The homogeneous deformation microstructures in the AT samples subjected to MDF to $\varepsilon\sim1.2$ are characterized by small values of grain/subgrain boundary misorientations providing large fractions of LABs. The number fractions of boundaries/subboundaries rapidly decrease with increase in their misorientation. The subsequent MDF is accompanied by a continuous formation of HABs, which are more readily developed at higher deformation temperature. The small peaks for grain boundary misorientations around 45° that evolved after MDF to $\varepsilon\geq2$ at 673 K suggest that the misorientation distribution of the deformation boundaries tends to approach random misorientation distribution as strain increases.

The effect of MDF at 300 K and 673 K on the structural changes in the AT samples is summarized in Fig. 10. Similar to the ST state, the mean grain size in the AT state rapidly decreases during MDF to $\varepsilon\sim2$, followed by a gradual reduction upon subsequent deformations. The mean grain size of 1.2 μm evolves during the MDF to $\varepsilon\sim4$ at 300 K, while the average grain size of 0.64 μm is obtained at 673 K. The transverse subgrain size and the dislocation density negligibly depend on the temperature. These parameters approach their final values just after the first forging pass at both temperatures. Then, the transverse subgrain size slightly decreases, while the dislocation density tends to increase during the MDF to large strain. The fractions of HABs and UFGs gradually increase during the MDF at 300 K, attaining the values of 0.28 and 0.15, respectively, at $\varepsilon\sim4$. Increasing the temperature to 673 K significantly accelerates the grain refinement kinetics, with $F_{HAB}=0.54$ and $F_{UFG}=0.59$ being obtained at $\varepsilon\sim4$. The increase in the fractions of the HABs and the UFGs during MDF at 673 K is characterized by a dramatic increase in the strain range of ~1.2 to ~2. Note that a similar behavior was observed for the ST state (Fig. 6). The rapid development of the UFGs in the strain range of 1–2 can be considered as a common feature of grain refinement in the Cu–Cr–Zr alloys during MDF at elevated temperatures.

3.4. Room temperature hardness and electro-conductivity

Fig. 11 summarizes the effect of MDF at 300 K and 673 K on the hardness (Hv) and electro-conductivity (κ) of the ST and AT samples. Generally, the change in the hardness correlates with the strain dependence of the flow stress during the MDF (Figs. 2 and 11a). Note that the hardness/flow stress ratio is 3.5 for MDF at 300 K and 5 for 673 K. The rate of strain hardening during MDF gradually decreases to almost zero with increasing total strain. The first forging pass results in drastic hardening of the ST state, whereas the hardening of the AT samples is not significant. Quantitatively, nearly the same Hv–ε dependencies are obtained in the strain range of 0.4–4 for the AT samples processed at both temperatures and for the ST samples processed at 673 K. Namely, the hardness of ~1500 MPa at $\varepsilon\sim0.4$ increases to ~1800 MPa with an increase of the total strain to 4. In contrast, the ST samples processed at 300 K are characterized by somewhat lower hardness levels compared to those strained at 673 K. It is clearly seen in Fig. 11a that the difference in the Hv between the ST samples subjected to MDF at 300 K and all the other samples is ~300 MPa in the strain range of 0.4–4.

The strain hardening of Cu–Cr–Zr alloys during MDF is accompanied by a decrease in their electro-conductivity (Fig. 11b). A reduction in the κ value of ~50% was observed after the first forging pass of the AT samples. In contrast, the ST samples do not demonstrate a

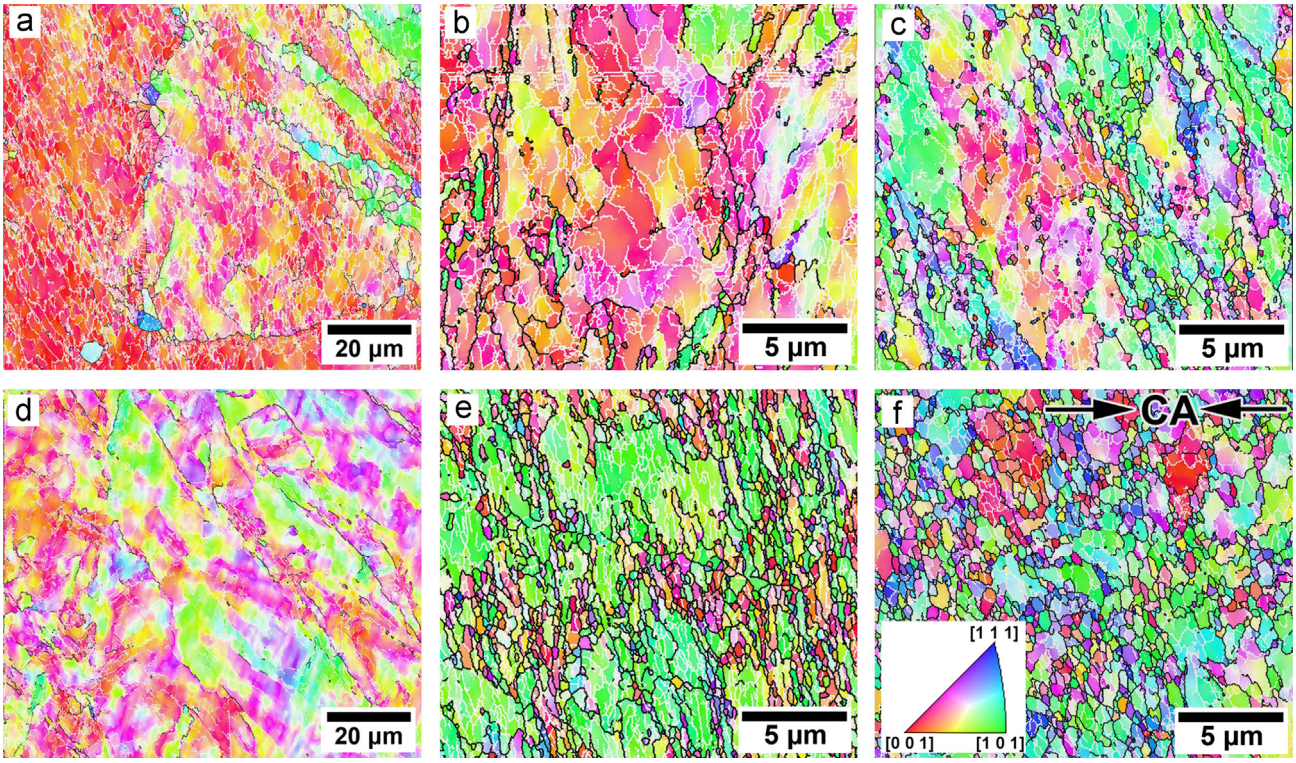

Fig. 7. Typical microstructures developed in the Cu–Cr–Zr alloy after the aging treatment (AT) during multidirectional forging at 300 K (a–c) and 673 K (d, e, f) to a total strain of 1.2 (a, d); 2 (b, e); and 4 (c, f). The white and black lines indicate the low- ($\theta < 15^{\circ}$) and high-angle ($\theta \geq 15^{\circ}$) boundaries, respectively. The inset in (f) shows the inverse pole figures for the compression axes (CA) in the last compression pass.

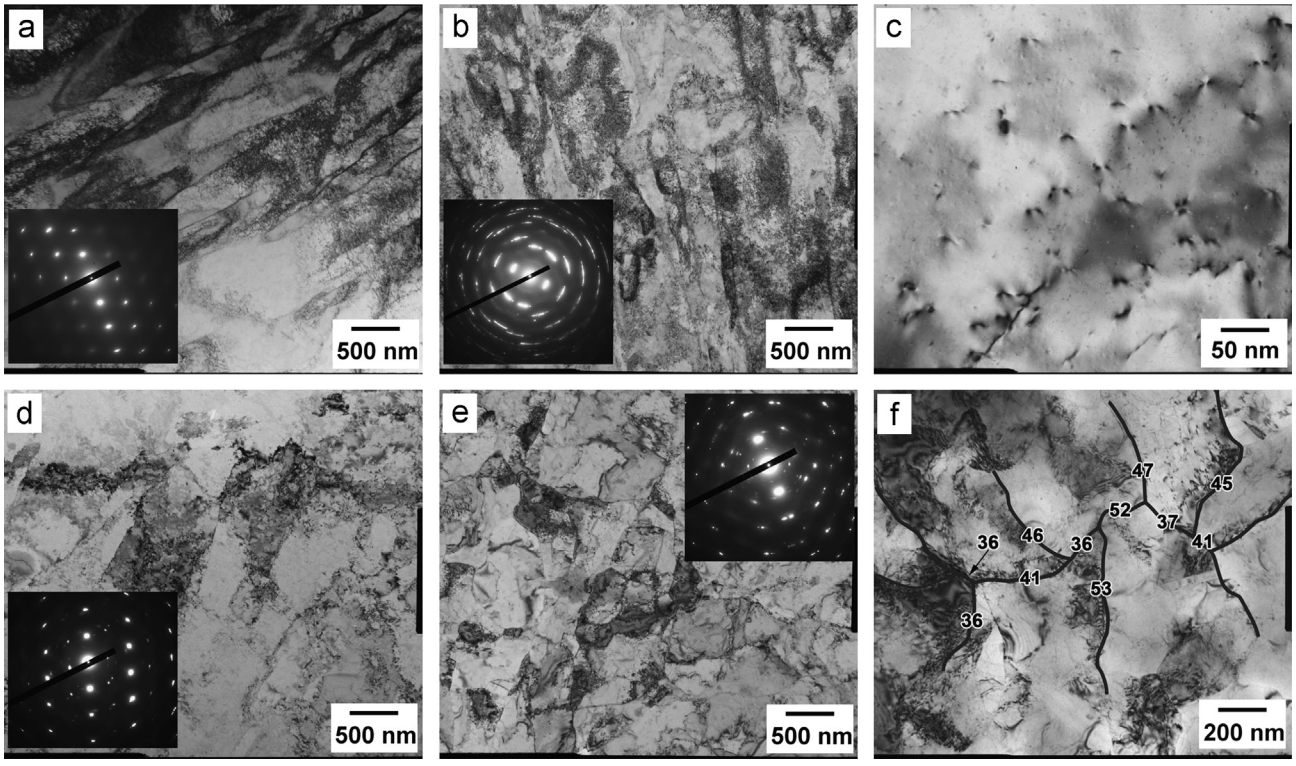

Fig. 8. Typical TEM micrographs of the Cu–Cr–Zr alloy in the peak aged condition (AT) subjected to multidirectional forging at 300 K to total strains of 0.4 (a); 2 (b); 1.2 (c) and at 673 K to total strains of 0.4 (d); 1.2 (e); and 4 (f).

remarkable change in the κ value at 673 K, although the first MDF pass at 300 K leads to a notable deterioration of the electro-conductivity for this material as well (Fig. 11b). Upon further MDF to $\varepsilon \sim 4$, the electro-conductivity gradually degrades irrespective of the initial state of the material and the processing temperature. The samples processed at 300 K are characterized by lower κ values than the samples forged at 673 K, and this difference is more pronounced in the ST samples.

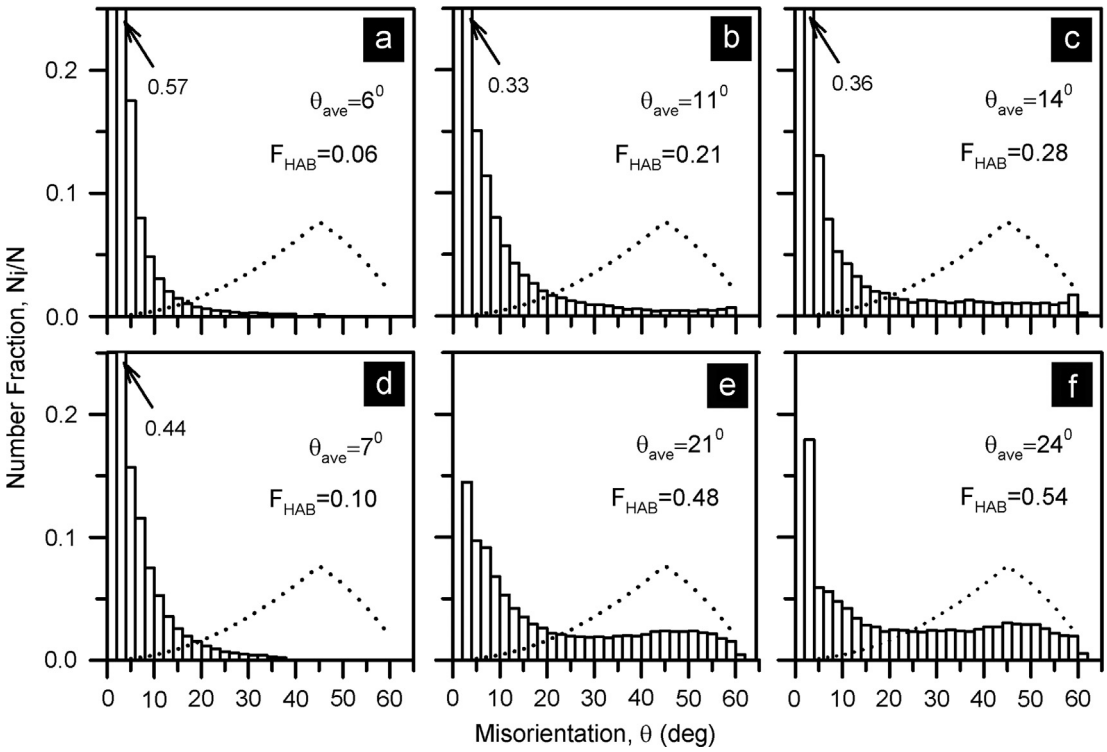

Fig. 9. Misorientation distributions of grain/subgrain boundaries in the Cu–Cr–Zr alloy in the aged condition (AT) subjected to multidirectional forging at 300 K (a–c) and 673 K (d–f) to a total strain of 1.2 (a, d); 2 (b, e); and 4 (c, f).

4. Discussion

4.1. Ultrafine grain development

The experimental results unambiguously demonstrate that microstructural evolution resulting in the formation of UFGs occurs through a type of continuous reactions in Cu–Cr–Zr alloy during MDF at 300 K and 673 K. The new grains form as a result of the increase in the misorientation of the LABs, which continuously accumulate the dislocations introduced by deformation and then progressively transform into HABs that are essentially CDRX [46]. The development of the present CDRX, which is actually a one-step process [46], can be considered to occur in three consecutive stages. At Stage I, the plastic working brings about high density dislocations, which arrange into the planar LABs. The deformation banding plays a very important role in the initial introduction of moderate-to-large misorientations. Geometrically necessary boundaries (GNBs) [46–49] delimiting the deformation bands rapidly increase their misorientations and, therefore, transform into HABs [46,50]. This transformation leads to the sub-division of the original grains into largely misoriented fragments. Sakai et al. [46,51] considered this process to be a mechanically driven one. At Stage II, the sub-division of the deformation bands due to the transverse boundaries result in the development of a spatial array of GNBs. The development of a spatial network of GNBs is promoted by the change in the forging direction from pass to pass. The elongated crystallites delimited by the GNBs rapidly evolve along the deformation bands. At Stage III, the number and misorientations of GNBs continuously increase with increasing cumulative strain, leading to the UFG development. Contrary to Stage I, the processes of UFG formation at Stages II and III are thermally activated ones [46,51]. Therefore, an increase in the MDF temperature accelerates the microstructural evolution. The faster kinetics of grain refinement at higher temperature may be attributed to facilitating the dynamic recovery at elevated temperature, which increases the number of GNBs that are able to acquire high-angle misorientation. Increasing temperature can accelerate full release of internal stresses, which are evolved by plastic working, and promote the dislocation rearrangement in the strain-induced boundaries, leading to the formation of perfect grain boundaries, much as early annealing changes the microstructure of severely deformed samples [52]. Note that the deformation microstructures are somewhat characterized by heterogeneities. The developed microstructure consists of UFGs and rather coarse remnants of the original grains, even at the largest strain attained in the present study.

The drastic increase in the dislocation density during the first forging pass is responsible for both the significant strengthening and the degradation of electric conductivity (cf. Figs. 6, 10 and 11). However, the dislocation density in grain/subgrain interiors is almost independent of strain at $\varepsilon \geq 0.4$ (Figs. 6 and 10). Therefore, the strengthening and the decreasing electrical conductivity upon further deformation can be attributed to the evolution of the HABs. It is known [53] that electron scattering on impurities, dislocations and grain boundaries contributes to electrical resistivity. The effect of the UFG formation and the dislocation density on the electrical conductivity is represented in Fig. 12. It is clearly seen in Fig. 12 that the UFG and HAB fractions have only a marginal effect on the electrical conductivity. In contrast, the electric conductivity almost linearly decreases with increasing the dislocation density. The present results suggest that the contribution of the dislocations to a decrease in the conductivity is significantly higher than that of the grain boundaries. Therefore, extensive grain refinement is an attractive method to achieve high strength and sufficient electrical conductivity in copper alloys. However, UFGs should contain a low dislocation density, which may be attained by subsequent recovery annealing.

4.2. Effect of dispersed particles

The MDF insignificantly affects the distribution of the secondary phase particles in the AT samples. In contrast, the MDF leads to partial decomposition of the supersaturated solid solution and precipitation of the nanoscale dispersoids in the ST state even at ambient temperature. As a result, at 300 K and $\varepsilon \sim 0.4$, the electrical

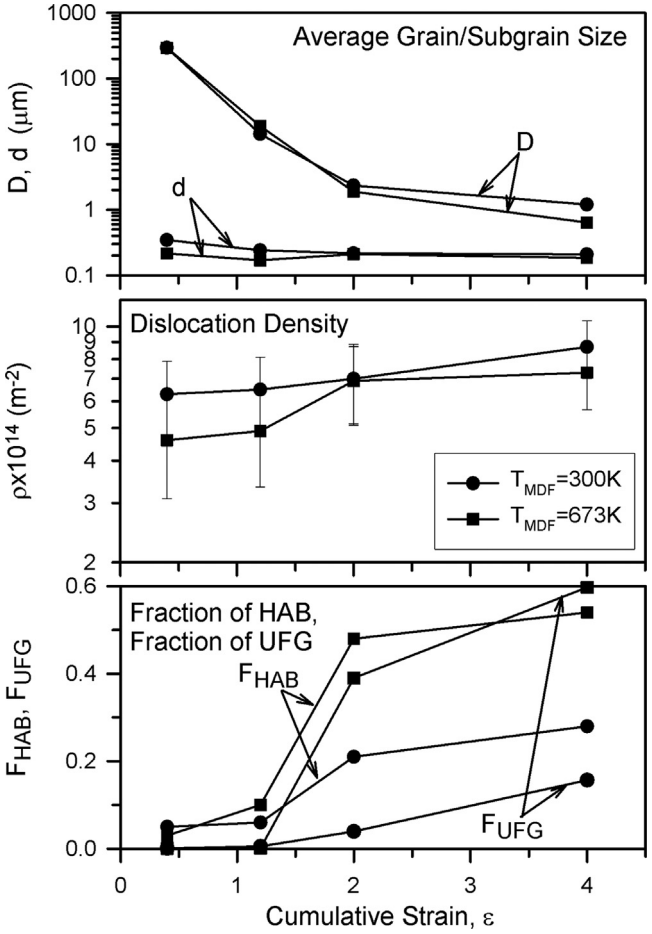

Fig. 10. Effect of multidirectional forging at 300 K and 673 K on the structural parameters (the average grain/(sub)grain size, (D, d), the dislocation density (ρ), the fraction of HAB (F_{HAB}) and the fraction of ultrafine grains (F_{UFG})) in the aging treated (AT) state of a Cu–Cr–Zr alloy.

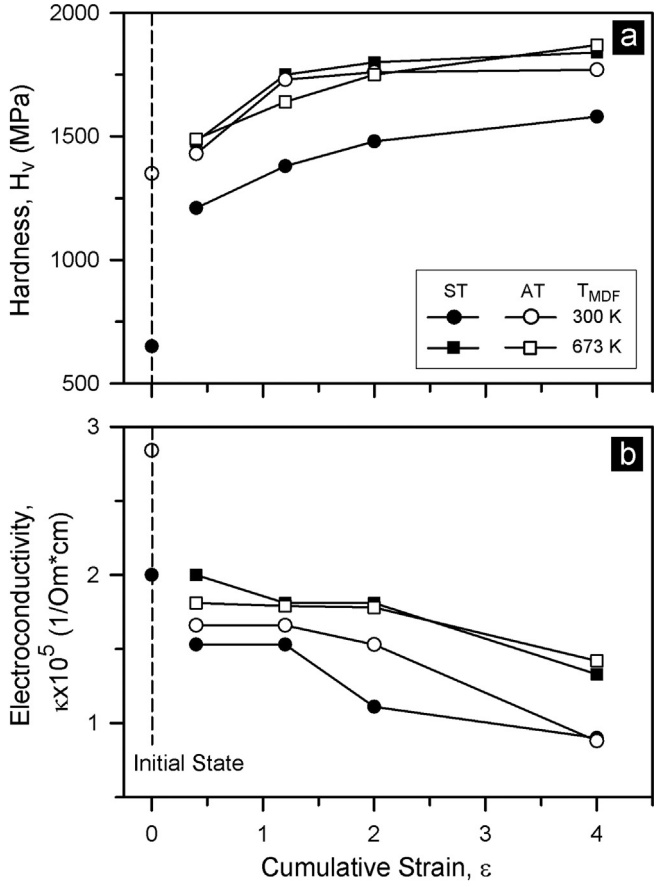

Fig. 11. Effect of multidirectional forging at 300 K and 673 K on the hardness (Hv) and electro-conductivity (κ) in the solution-treated and aged samples of Cu–Cr–Zr alloy.

conductivity decreases by 40% in the AT state and by 25% in the ST state (Fig. 11), despite the nearly identical dislocation density in these materials (Figs. 6 and 10). It is obvious that a decrease in electron scattering on impurities partially compensates for the increase in electron scattering on dislocations in the ST samples.

At 300 K, the initial dispersion of the secondary phases does not have any remarkable influence on the grain refinement. The final fractions of the UFGs are very small, as they do not exceed 0.2 even at $\varepsilon \sim 4$ in both the ST and AT states. The nearly identical kinetics of grain refinement in the ST and AT states might be associated with the strain-induced precipitation of the dispersed particles in the ST state. However, the decomposition of the supersaturated solid solution in the ST state is incomplete, even at $\varepsilon \sim 4$, because the AT state is characterized by slightly higher values of both the electro-conductivity and the flow stress/hardness compared to the ST state (Figs. 2 and 11). This result suggests that the difference in the precipitates between the ST and AT states is retained during the MDF at ambient temperature.

In contrast, at 673 K, initial dispersion of nanoscale precipitation is favorable for the UFG development in Cu–Cr–Zr alloy. The area fraction of the UFGs is remarkably larger in the AT state than that in the ST state, i.e., 0.59 against 0.36 at $\varepsilon \sim 4$ (Figs. 6 and 10). Note that in the ST state, the strain-induced decomposition of solid solution readily occurs and completes at $\varepsilon \sim 1.2$, taking into account that the values of electrical conductivity, flow stress and microhardness in the ST and AT states become the same (Figs. 2 and 11). Therefore, the dispersions of the secondary phase particles in both the ST and AT states after MDF with a cumulative strain of ~ 1.2 at 673 K become nearly the same. The differences in the flow stress (Fig. 2) and electrical conductivity (Fig. 11) between the ST and AT samples were observed during the first forging pass only.

Nevertheless, the previous aging treatment provided more homogeneous microstructure evolution in the AT state. Obviously, the initial presence of finely dispersed particles resulted in homogeneous deformation during the first forging pass, leading to a rather uniform distribution of strain-induced low-angle GNBs, which are able to acquire high-angle misorientations during subsequent deformation. Then, a massive fraction of the UFGs appeared after sufficiently large strains due to progressive transformation of these low-angle GNBs into HABs. In contrast, a limited number of inhomogeneously distributed GNBs evolved in the ST state at $\varepsilon \sim 0.4$, leading to local development of the UFGs upon further straining. Therefore, the uniform formation of GNBs within the initial grains highly promotes the further grain refinement at large strains.

5. Conclusions

The structural changes leading to ultrafine grain development in a Cu–0.3%Cr–0.5%Zr alloy during multidirectional forging at 300 K and 673 K were studied for both quenched aged samples. The primary results can be summarized as follows:

1. At small strains of $\varepsilon \leq 1.2$, a rapid increase in the flow stress occurs. An apparent steady-state flow is attained at strains of $\varepsilon \geq 2$. The samples previously subjected to aging treatment were characterized by higher flow stresses during deformation at 300 K compared to those after solution treatment, while

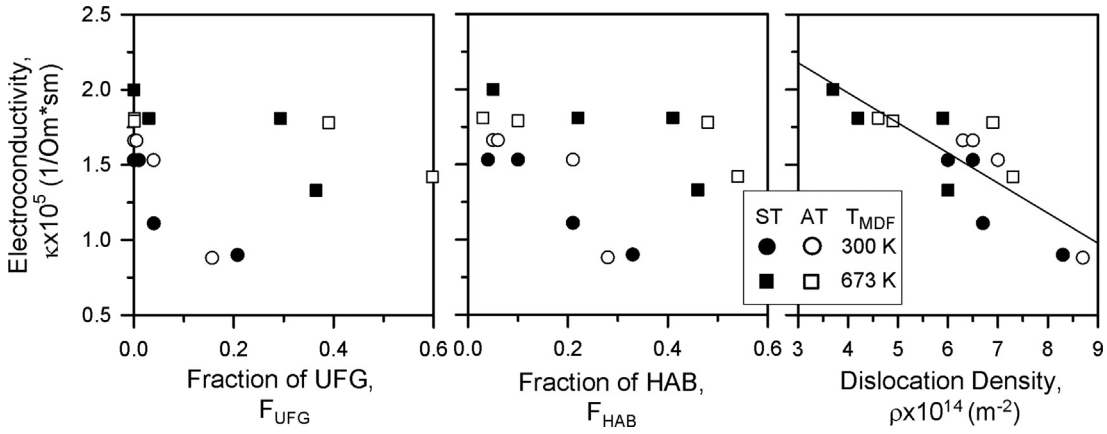

Fig. 12. Effects of the UFG fraction (F_{UFG}), the HAB fraction (F_{HAB}) and the dislocation density (ρ) on the electric conductivity (κ) of Cu–Cr–Zr alloy.

almost the same level of flow stresses and hardness was recorded at 673 K for both the solution and the samples after the aging treatment.

2. The structural changes were associated with the development of continuous dynamic recrystallization. After 10 consequent forging passes to a total strain of 4 at 300 K, the mean grain sizes of 1.4 μm and 1.2 μm were obtained in the solution-treated and the aged samples, respectively. The same processing at 673 K resulted in the mean grain sizes of 0.9 μm in the solution-treated samples and 0.6 μm in the aged samples.
3. An increase in the deformation temperature promoted the ultrafine grain formation. The area fractions of ultrafine grains with a size below 2 μm were 0.2 and 0.15 in the initial solution treated and aged samples, respectively, after straining to $\varepsilon \sim 4$ at 300 K. The area fractions of ultrafine grains comprised 0.36 and 0.59 in the solution treated and aged samples, respectively, after straining to $\varepsilon \sim 4$ at 673 K.

Acknowledgments

The financial support received from the Ministry of Education and Science, Russia, under Grant no. 14.740.11.0849 is gratefully acknowledged. The authors are grateful to the personnel of the Joint Research Centre, Belgorod State University, for their assistance with instrumental analysis.

References

[1] L. Lu, Y. Shen, X. Chen, L. Qian, K. Lu, Science 304 (2004) 422–426.
[2] I.S. Batra, G.K. Dey, U.D. Kulkarni, S. Banerjee, J. Nucl. Mater. 299 (2001) 91–100.
[3] H.T. Zhou, J.W. Zhong, X. Zhou, Z.K. Zhao, Q.B. Li, Mater. Sci. Eng. A 498 (2008) 225–230.
[4] X.F. Li, A.P. Dong, L.T. Wang, Z. Yu, L. Meng, J. Alloys Compd. 509 (2011) 4092–4097.
[5] N.D. Stepanov, A.V. Kuznetsov, G.A. Salishchev, N.E. Khlebova, V.I. Pantsyrny, Mater. Sci. Eng. A 564 (2013) 264–272.
[6] A. Singh, L. Tang, M. Dao, L. Lu, S. Suresh, Acta Mater. 59 (2011) 2437–2446.
[7] A. Vinogradov, T. Ishida, K. Kitagawa, V.I. Kopylov, Acta Mater. 53 (2005) 2181–2192.
[8] F. Dalla Torre, R. Lapovok, J. Sandlin, P.F. Thomson, C.H.J. Davies, E.V. Pereloma, Acta Mater. 52 (2004) 4819–4832.
[9] Z.J. Zhang, Q.Q. Duan, X.H. An, S.D. Wu, G. Yang, Z.F. Zhang, Mater. Sci. Eng. A 528 (2011) 4259–4267.
[10] A. Mishra, B.K. Kad, F. Gregori, M.A. Meyers, Acta Mater. 55 (2007) 13–28.
[11] N. Takata, Y. Ohtake, K. Kita, K. Kitagawa, N. Tsuji, Scr. Mater. 60 (2009) 590–593.
[12] D.J. Edwards, B.N. Singh, S. Tahtinen, J. Nucl. Mater. 367–370 (2007) 904–909.
[13] J-H. Su, Q-M. Dong, P. Liu, H-J. Li, B-X. Kang, Mater. Sci. Eng. A 392 (2005) 422–426.
[14] H.T. Zhoua, J.W. Zhonga, X. Zhoub, Z.K. Zhaoa, Q.B. Li, Mater. Sci. Eng. A 498 (2008) 225–230.
[15] A. Belyakov, M. Murayama, Y. Sakai, K. Tsuzaki, M. Okubo, M. Eto, T. Kimura, J. Electron. Mater. 35 (2006) 2000–2008.
[16] K.X. Wei, W. Wei, F. Wang, Q.B. Dua, I.V. Alexandrov, J. Hu, Mater. Sci. Eng. A 528 (2011) 1478–1484.
[17] A. Vinogradov, V. Patlan, Y. Suzuki, K. Kitagawa, V.I. Kopylov, Acta Mater. 50 (2002) 1639–1651.
[18] A. Chibihi, X. Sauvage, D. Blavette, Acta Mater. 60 (2012) 4575–4585.
[19] H. Fuxiang, M. Jusheng, N. Honglong, G. Zhiting, L. Chao, G. Shumei, Y. Xuetao, W. Tao, L. Hong, L. Huafen, Scr. Mater. 48 (2003) 97–102.
[20] G.B. Lin, Z.D. Wang, M.K. Zhang, H. Zhang, M. Zhao, Mater. Sci. Technol. 27 (2011) 966–969.
[21] I.S. Batra, G.K. Dey, U.D. Kulkarni, S. Banerjee, Mater. Sci. Eng. A 356 (2002) 32–36.
[22] W.X. Qi, J.P. Tu, Y.Z. Yang, Mater. Sci. Eng. A 343 (2003) 89–96.
[23] T. Fujii, H. Nakazawa, M. Kato, U. Dahnem, Acta Mater. 48 (2000) 1033–1045.
[24] J. Su, P. Liu, H. Li, F. Ren, Q. Dong, Mater. Lett. 61 (2007) 4963–4966.
[25] A.P. Zhilyaev, T.G. Langdon, Prog. Mater. Sci. 53 (2008) 893–979.
[26] R.Z. Valiev, T.G. Langdon, Prog. Mater. Sci. 51 (2006) 881–981.
[27] Y. Estrin, A. Vinogradov, Acta Mater. 61 (2013) 782–817.
[28] K. Valdés León, M.A. Munoz-Morris, D.G. Morris, Mater. Sci. Eng. A 536 (2012) 181–189.
[29] J. Wongsa-Ngama, M. Kawasaki, T.G. Langdon, Mater. Sci. Eng. A 556 (2012) 526–532.
[30] C.Z. Xu, Q.J. Wang, M.S. Zheng, J.W. Zhu, J.D. Li, M.Q. Huang, Q.M. Jia, Z.Z. Du, Mater. Sci. Eng. A 459 (2007) 303–308.
[31] J. Wongsa-Ngama, M. Kawasaki, T.G. Langdon, J. Mater. Sci. 48 (2013) 653–4660.
[32] J. Wongsa-Ngama, M. Kawasaki, Y. Zhao, T.G. Langdon, Mater. Sci. Eng. A 528 (2011) 7715–7722.
[33] J. Wongsa-Ngama, H. Wen, T.G. Langdon, Mater. Sci. Eng. A 579 (2013) 126–135.
[34] A. Belyakov, T. Sakai, H. Miura, K. Tsuzaki, Philos. Mag. A 81 (2001) 2629–2643.
[35] A. Belyakov, W. Gao, H. Miura, T. Sakai, Metall. Mater. Trans. 29A (1998) 2957–2965.
[36] A. Belyakov, T. Sakai, H. Miura, R. Kaibyshev, ISIJ Int. 39 (1999) 592–599.
[37] E. Brunger, X. Wang, G. Gottstein, Scr. Mater. 38 (1998) 1843–1849.
[38] S. Gourdet, F. Montheillet, Acta Mater. 51 (2003) 2685–2699.
[39] A. Belyakov, K. Tsuzaki, H. Miura, T. Sakai, Acta Mater. 51 (2003) 847–861.
[40] A. Belyakov, T. Sakai, R. Kaibyshev, Metall. Mater. Trans. 29 (1998) 161–167.
[41] P.B. Hirsch, A. Howie, R.B. Nicholson, D.W. Pashley, M.J. Whelan, Electron Microscopy of Thin Crystals, second ed., Krieger, New York, 1977.
[42] A. Korbel, J. Rys, M. Szczerba, Acta Metall. 33 (1998) 2215–2219.
[43] F.J. Humphreys, M. Hatherly, Recrystallization and Related Annealing Phenomena, Elsevier, Oxford, 2005.
[44] O. Sitdikov, T. Sakai, E. Avtokratova, R. Kaibyshev, K. Tsuzaki, Y. Watanabe, Acta Mater. 56 (2008) 821–834.
[45] J.K. Mackenzie, Biometrika 45 (1958) 229–240.
[46] T. Sakai, A. Belyakov, R. Kaibyshev, H. Miura, J.J. Jonas, Prog. Mater. Sci. 60 (2014) 130–207.
[47] D.A. Hughes, N. Hansen, D.J. Bammann, Scr. Mater. 48 (2003) 147–153.
[48] G. Winther, X. Huang, A. Godfrey, N. Hansen, Acta Mater. 52 (2004) 4437–4446.
[49] Y. Huang, J.D. Robson, P.B. Prangnell, Acta Mater. 58 (2010) 1643–1657.
[50] W. Pantleon, Acta Mater. 46 (1998) 451–456.
[51] T. Sakai, A. Belyakov, H. Miura, Metall. Mater. Trans. 39A (2008) 2206–2214.
[52] C. Kobayashi, T. Sakai, A. Belyakov, H. Miura, Philos. Mag. Lett. 87 (2007) 751–766.
[53] A.P. Zhilyaev, I. Shakhova, A. Belyakov, R. Kaibyshev, T.G. Langdon, Wear 305 (2013) 89–99.